Supplement of Solid Earth, 11, 1681–1698, 2020
https://doi.org/10.5194/se-11-1681-2020-supplement

Solid Earth Open Access EGU

Supplement of

New insights into active tectonics and seismogenic potential of the Italian Southern Alps from vertical geodetic velocities

Letizia Anderlini et al.

Correspondence to: Letizia Anderlini (letizia.anderlini@ingv.it)

Text S1. GPS Data Processing

The position time-series have been obtained adopting a three-step procedure approach, as in Serpelloni et al. (2006), that includes: 1) raw phase data reduction, 2) combination of loosely constrained network solutions and reference frame definition and 3) time-series analysis, including velocity estimates and spatial filtering of common mode errors.

The raw GPS observables have been analyzed using the 10.6 version of the GAMIT/GLOBK package (Herring et al., 2015) adopting standards defined in the framework of the IGS "Repro2 campaign" (http://acc.igs.org/reprocess2.html). The GAMIT software is used to estimate station positions, atmospheric delays, satellite orbits, and Earth orientation parameters from ionosphere-free linear combination GPS phase observables using double differencing techniques to eliminate phase biases caused by drifts in the satellite and receiver clock oscillators. GPS pseudo-range observables are used to constrain clock timing offsets and to improve automated editing of the phase data, assisting in the resolution of integer phase ambiguities. GPS phase data are weighted according to an elevation-angle-dependent error model (Herring et al., 2015) using an iterative analysis procedure whereby the elevation dependence is determined from the observed scatter of phase residuals.

In this analysis the satellites orbit parameters are fixed to the IGS final products. We use the IGS absolute antenna phase center model for both satellite and ground- based antennas, which improves the accuracy of estimates for the vertical components of site position by mitigating reference frame scale and atmospheric mapping function errors (e.g., Schmid et al., 2005, 2007). While the first-order ionospheric delay is eliminated by the ionosphere-free linear combination, the second-order ionospheric corrections are applied based on the formulation of Petrie et al. (2010), using IONEX files from the Center for Orbit Determination in Europe (CODE). The tropospheric delay is modeled as piecewise linear model and estimated using the Vienna Mapping Function 1 (VMF1; Boehm et al., 2006) with a 10° cutoff. We use the Global Pressure and Temperature 2 (GPT2; Lagler et al., 2013) model to provide a priori hydrostatic delays. The pole tide was also corrected in GAMIT by IERS standards. The Earth Orientation Parameters (EOP) are tightly constrained to priori values obtained from IERS Bulletin B. Non-tidal atmospheric loading and ocean tidal loading are corrected using MIT filtered atmospheric displacements files (available at ftp://everest.mit.edu/pub/GRIDS) and the FES2004 (Lyard et al., 2006) model, respectively. The International Earth Rotation Service (IERS) 2003 model for diurnal and semi-diurnal solid Earth tides was set.

Because of the large number of stations included in our Euro-Mediterranean GPS processing (~3000), this step is performed for several sub-networks, each made by <50 stations, with each sub-network sharing a set of high-quality IGS stations, which are used as tie-stations in the combination step.

In the second step we use the ST_FILTER program of the QOCA software (http://qoca.jpl.nasa.gov), which adopts a Kalman filter estimation algorithm (Dong et al., 1998, 2002), to combine all the daily

loosely constrained solutions with the global solution of the IGS network made available by MIT (http://sopac.ucsd.edu), and simultaneously realize a global reference frame by applying generalized constraints (Dong et al., 1998). Specifically, we define the reference frame by minimizing the velocities of the IGS core stations (http://igscb.jpl.nasa.gov), while estimating a seven- parameter transformation with respect to the GPS realization of the ITRF2008 frame (Altamimi et al., 2011), i.e., the IGb08 reference frame.

In the third step we analyze the position time series in order to estimate and correct offsets due to stations equipment changes, while simultaneously estimating annual and semi-annual periodic signals and a linear velocity term. In this analysis we retain only data from GPS stations with an observation period longer than 2.5 years, as shorter intervals may result in biased estimates of linear velocities (Blewitt and Lavallée, 2002). The model derived from the combination of these signals is then subtracted from the position time series in order to get the residual positions. The residual time-series are then used to estimate the Common Mode Error (CME) performing a Principal Component Analysis (PCA), as described in Dong et al. (2006). The PCA is performed at a continental-scale, over the same area used by Serpelloni et al. (2013), and the first two PCs are here considered as CME. This prevents the removal of the eventual more localized signals of geophysical interests recorded by the GPS stations in the study region, since the PCA detects the signals common to a much larger region. As a result, after removing the CME, the typical repeatability in our analysis is ~1 mm for the horizontal components, and ~3 mm for the vertical component, with a 30% gain in the daily repeatability and a significant improvement of the signal to noise ratio. After the spatial filtering, the estimated seasonal motions are added back to the filtered time-series, obtaining position time series with a reduced scatter around the adopted model.

Text S2. InSAR Data Processing

The InSAR data processing has been performed using the SARScape module of ENVI software, provided by Harris Geospatial Solutions (http://sarmap.ch/tutorials/sbas_tutorial_V_2_0.pdf), to perform SBAS analysis. The SBAS algorithm includes several steps (e.g Pasquali et al. 2014): creation of a connection graph (computing all differential interferograms from the input image stack according to the chosen criteria for temporal and geometric baselines), differential interferogram generation (spectral shift and adaptive filtering), phase unwrapping, orbit refinement and re-flattening, first estimation of the average displacement, atmospheric phase screen removal, and final estimation of the average displacement and mean ground velocity. In our study, we achieved a ground resolution of 90 m by using a multi-looking factor of 4 in range and 20 in the azimuth. All the Single Look Complex images (SLC) are co-registered in the master image geometry using a 90-m Digital Elevation Model (DEM) provided by the Shuttle Radar Topography Mission (SRTM). The

topographic phase contribution was removed using the DEM, too. We applied the Goldstein filter (Goldstein and Werner, 1998) to smooth the differential phase and use precise DORIS orbits (provided by the European Space Agency) and the SRTM DEM to correct the computed interferograms from possible orbital ramps. We used the Delauney minimum cost flow (MCF) network (Constantini, 1998) along with the Delaunay method to unwrap the differential interferograms. This method helps the propagation of the unwrapping solution to reach coherent pixels also if they are separated by non-coherent areas. The unwrapping coherence threshold at this stage was set to 0.3. We selected approximately several tens Ground Control Points (GCP) mainly at the borders of the processed frame, to perform the refinement and re-flattening step. Subsequently, the average displacement rate and residual height-correction factors were estimated by inverting a linear system through the Singular Value Decomposition method. Then, low-pass and high-pass spatial filters were used for the time-series images, to screen and remove the atmospheric phase component. In fact, the starting idea is that atmosphere is correlated in space but not in time. We considered two moving windows of 365 days and 1200 meters for the two filters (High and low pass). Finally, the solution of the inversion was geocoded through the used DEM. All of the final displacement measurements were obtained onto the satellite line of sight (LOS) direction and geocoded in the UTM 33N reference system.

Text S3. Vertical Leveling Data

The IGMI leveling campaigns have been performed following the International Geodetic Association standards defined in Oslo in 1948 (Vignal, 1936; 1950) that allows to have a high level accuracy of the final vertical rates. The considered leveling line is composed by almost a hundred benchmarks starting from the fixed one in Mestre (Venice) moving northward up to Fadalto valley and Val Belluna within the Venetian Eastern Southern Alps. The elevation changes measured during the campaign time interval (1952-1984) are reported in Table S2 along with the distance with respect to the reference benchmark and the position of each one in latitude and longitude. The available information on the levelling campaigns are only in terms of the final estimates of elevation values for each benchmark, without any notes about the discrepancy value obtained between forward and backward levelling measurements line, about the presence of any systematic errors and if any adjustment or correction has been applied during measurements procedures. In order to evaluate a reliable error associated with the elevation change estimate, we use the formula proposed by D'Anastasio et al. (2006):

$$e_i = \pm \sqrt{2 \sum_{j=1}^{i} (\sigma \sqrt{l_j})^2}$$

where l_i is the distance (in km) between consecutive benchmarks (thus $\sum_{j=1}^{i} l_j = L_i$ indicates the distance of each benchmark from the reference one) and σ is the maximum allowed discrepancy between forward and backward levelling line standard error of a 1 km long levelled segment, for which we use the value of 2.5 $\frac{mm}{\sqrt{km}}$ (D'Anastasio et al., 2006). The propagated error e_i indicates the error between the fixed benchmark and the i-th benchmark, representing the maximum allowable random error propagation (D'Anastasio et al., 2006). The propagated error is graphically depicted in Fig. S3A with the two continuous curves that allow to evaluate which elevation changes can be considered significant with respect to this maximum allowable random error. The error of the elevation change rate has been calculated considering the time interval of measurements (Δt = 32 years) as follows: $e_{ECi} = \frac{e_i}{\Delta t}$ (see Table S2 and Figure S3B).

Text S4. Subsampling InSAR data method

The method used to subsample InSAR datasets is based on the pixel density. The number of InSAR pixel is reduced maintaining the information of deformation provided by the original velocity field. We take into account the original area covered by the InSAR frame as the rectangle identified by the minimum and maximum values of latitude and longitude of InSAR pixels. We subdivide this rectangle into sub-portions until within each one there's a number of pixel lower than a reference one, n_{crit}. At this point each sub-portion is represented by just one pixel whose associated longitude, latitude and velocity are calculated as the median values of the enclosed pixels. The subsampling has been performed for both the ascending and descending solutions just on a portion of the InSAR dataset that is a 35 km wide stripe across the Montello and Bassano-Valdobbiadene thrusts along the NNW direction (see Figure S4). Considering two iterations of subdivisions, we define the number of divisions along longitude and latitude assuming two parameters:

1. the final number of pixel we want to obtain after the subsampling, *Np*;
2. the percentage of area, *R,* covered by the original InSAR data with respect to the initial rectangle.

For the first parameter we considered the same number for both datasets in order to do not have any predominance of one to the other, and to have a final dataset of few thousands of points that do not generate too much high computational costs. The second value is a more empirical estimate that could vary from 20% to 45%. The two parameters are related to each other in order to define the total number of subcells at the end of the two iterations. This means that if we want *Np* final points for an initial dataset that covers the starting region of *R* percentage, the subdivision along longitude (div_{lon}) and along latitude (div_{lat}) are such that the following relation is valid:

$$\frac{N_p}{R} = (div_{lon} * div_{lat})^2$$

Along this rationale, we define the two parameters div_{lon} and div_{lat} by trial and error in order to get the most equal number *Np* possible for the two datasets. For each settled div_{lon} and div_{lat} we define the critical number of pixel, n_{crit}, below which the cell is not further subdivided, as follows:

$$n_{crit} = \frac{T_p}{div_{lon} * div_{lat}}$$

where *Tp* indicates the initial number of pixel of the InSAR dataset.

The specific parameters considered in each subsampling for both the ascending and descending datasets are reported in Table S3.

Text S5. Long wavelength vertical velocity correction

We made a test by inverting for slip-rates and locking-depths assuming the same fault geometry (Fig. 6), but geodetic rates corrected for a long-wavelength vertical signal, which is here assumed as a linear gradient of uplift rate along 100 km of distance. Considering the mean uplift rate of 1 mm/year in the northernmost sector of the study area (the Dolomites), we choose 0.8 mm/year (80% of the uplift amount, from Sternai et al., 2019) as maximum vertical isostatic adjustment to be removed from the observed vertical velocities. In particular we consider a linear trend (with a slope of 0.008 mm/(year*km)) that starts from Treviso city (TREV and TVSO GPS stations), along the same direction of the profile indicated in Fig. 2, and reaching the limit of 0.8 mm/year of uplift rate in correspondence of POZZ station.

This vertical linear signal has been removed from all the geodetic datasets, i.e. from the vertical component of GPS velocities, leveling data and subsampled InSAR LoS rates, and it has been performed the inversion of the modified velocities in order to estimate locking depths and slip rates for the proposed fault geometry. Due to these changes in the input observations, we re-evaluate the relative weighting factor Wsar, finding an optimal value of 0.68.

The results of the inversion are presented in the Figure S10, showing the same information reported in Figure 7 of the manuscript with a few differences: the purple line in the section of the vertical rates represents the linear gradient we removed, and light gray dots indicate the unmodified original datasets, while all the other data are corrected for the linear gradient. The estimated parameters (locking depth and dip-slip rates) are reported in Figure S10 and in the following table.

LD Montello Ramp	LD Bassano Ramp	Slip rate Montello Ramp	Slip rate Montello Flat	Slip rate Bassano Ramp	Slip rate Deep Ramp	RMSE GPS	RMSE LEV	RMSE InSAR
4.6 km	8.6 km	0.5 mm/a	0.35 mm/a	2.0 mm/a	2.3 mm/a	0.46 mm/a	0.57 mm/a	0.59 mm/a

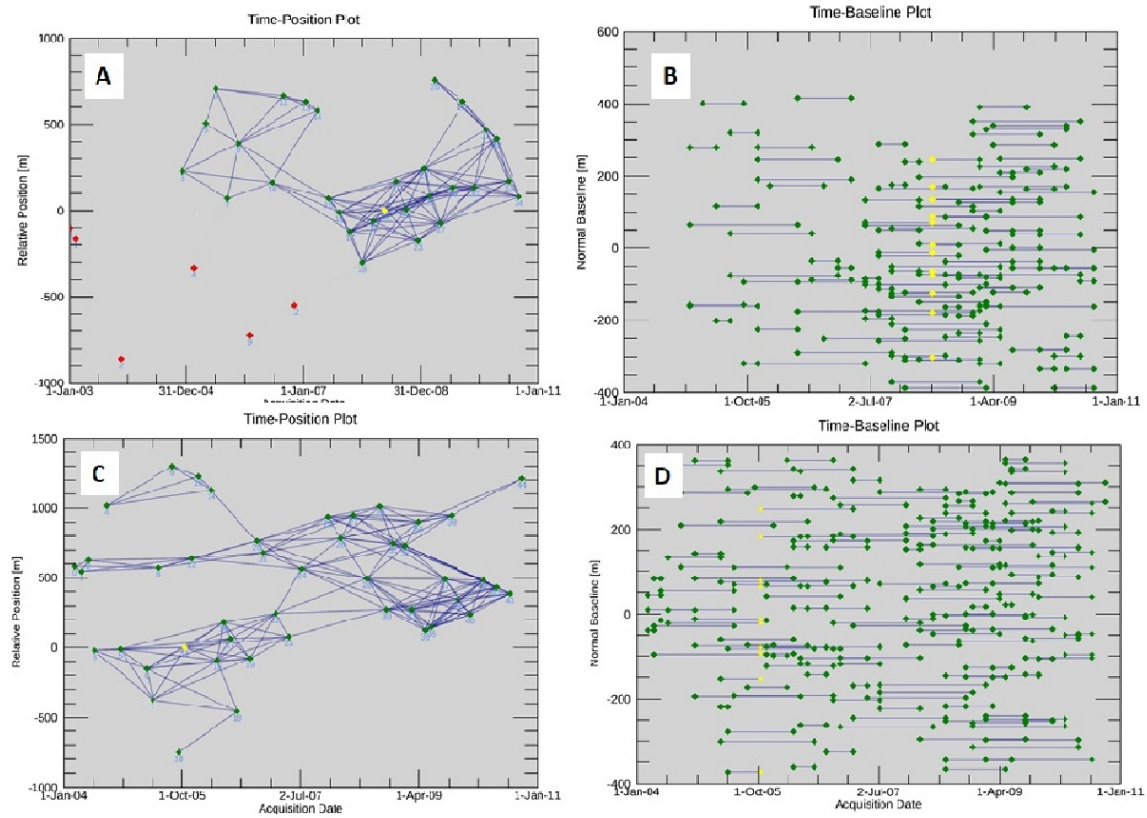

Figure S1 (A) Considered pairs connection graph for the descending SAR orbit; (B) Considered baseline graph for the descending SAR orbit; (C) Considered connection graph for the ascending SAR orbit; (D) Considered baseline graph for the ascending SAR orbit.

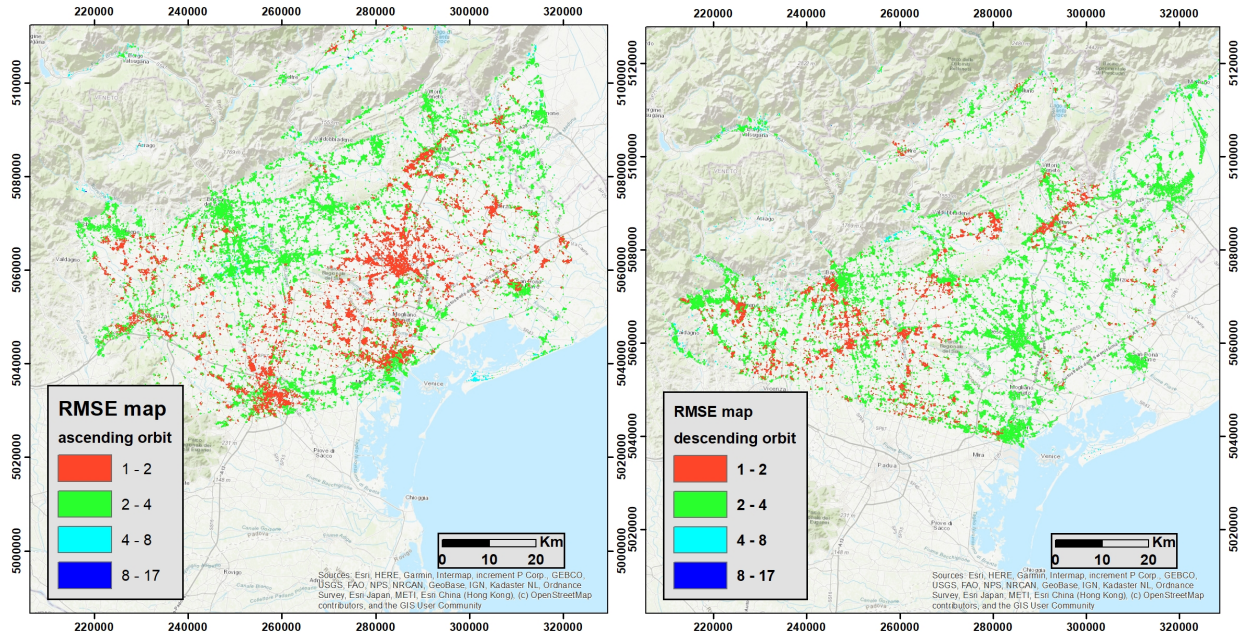

Figure S2 RMSE (mm) maps of the displacement time series for the ascending and descending orbits, computed as follows: $RMSE = \sqrt{(1-r2)} * SDy$, where SDy is the standard deviation of each retrieved

displacement time series and r is the correlation coefficient between the time series and the considered acquisitions.

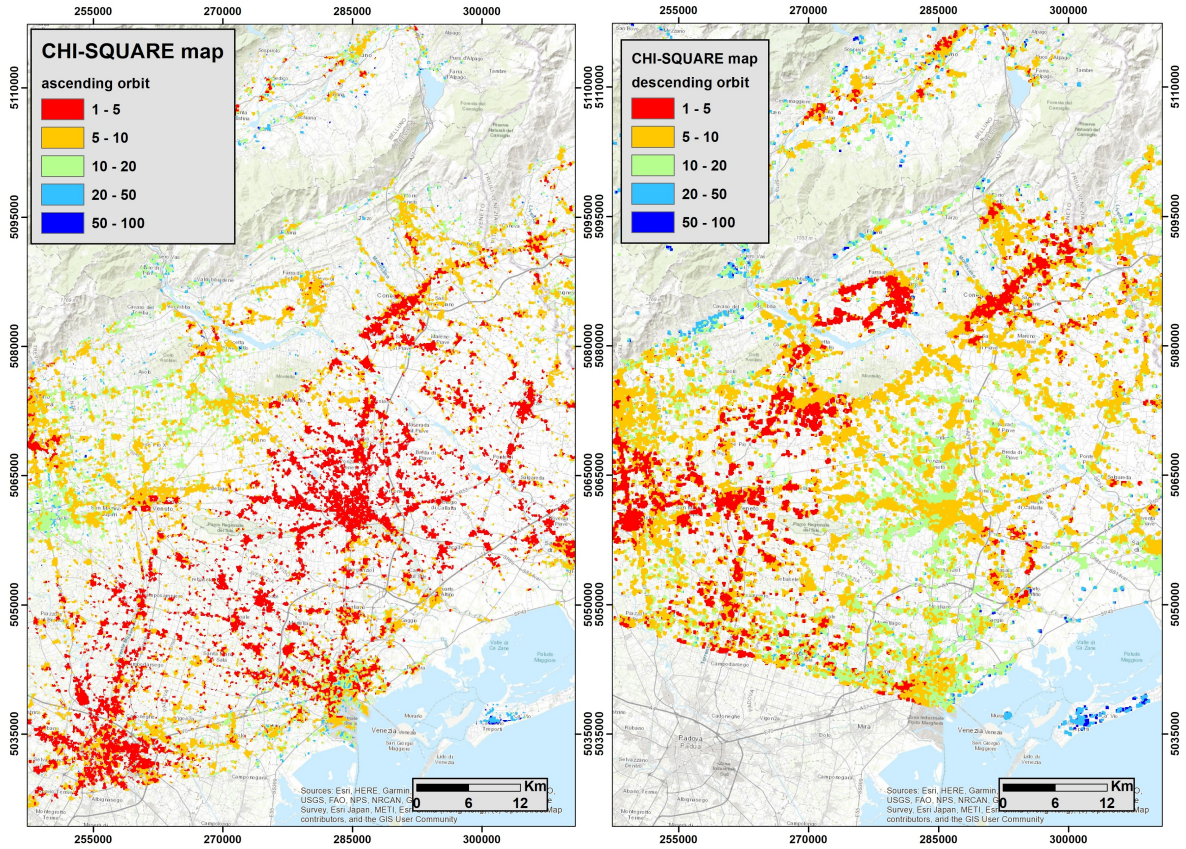

Figure S3 Chi-Square values for the ascending and descending orbits of the displacement time series with respect to a linear trend.

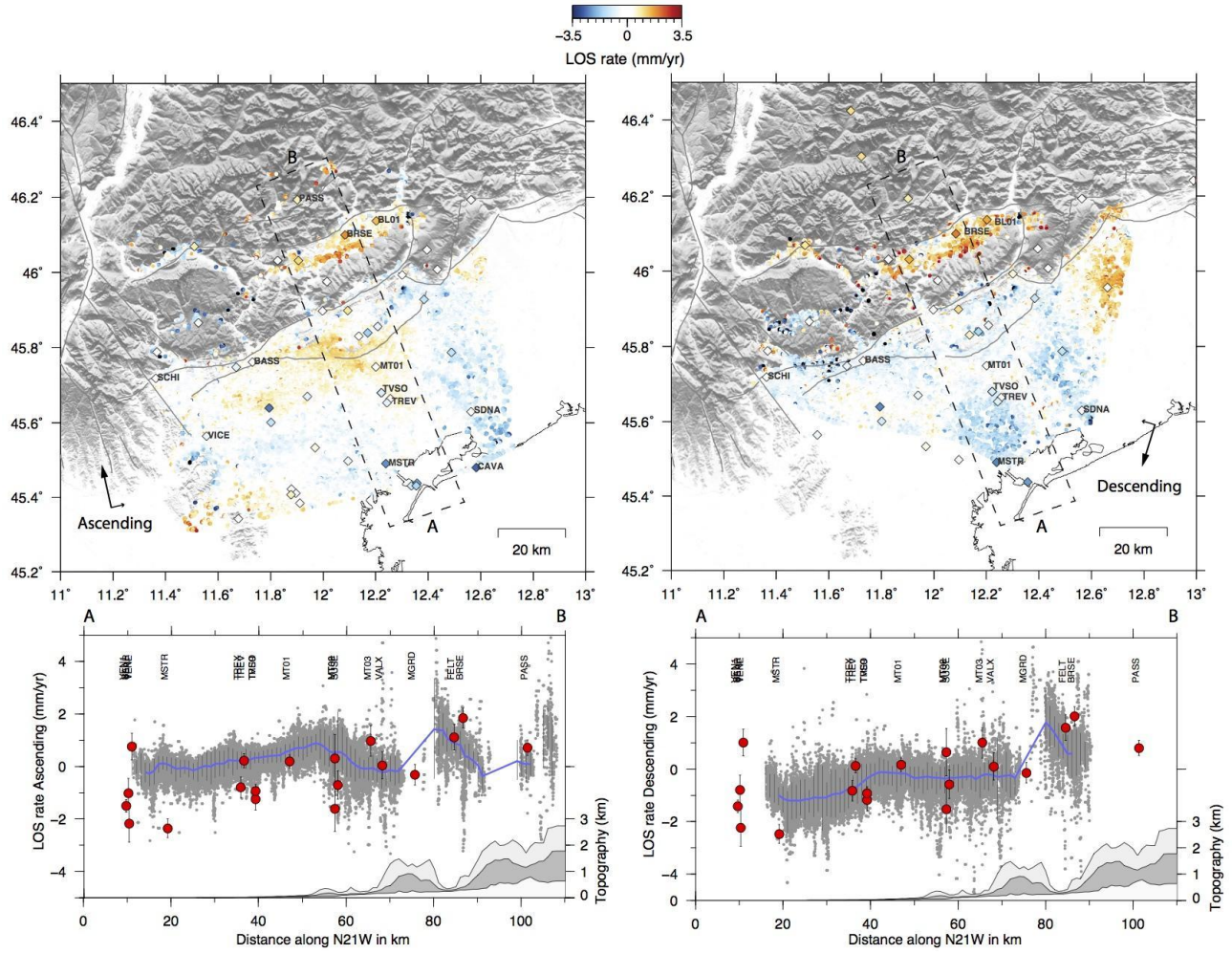

Figure S4 InSAR line-of-sight (LOS) velocities for the ascending (left) and descending (right) orbits, with negative (blue) and positive (red) values indicating increasing and decreasing distance between the Earth surface and the satellite. Colored diamonds indicate the 3D GPS velocities projected along the SAR LOS directions. Bottom panels show the SAR and GPS LOS velocities along the A-B cross section (dashed box) for the ascending and descending orbits, respectively.

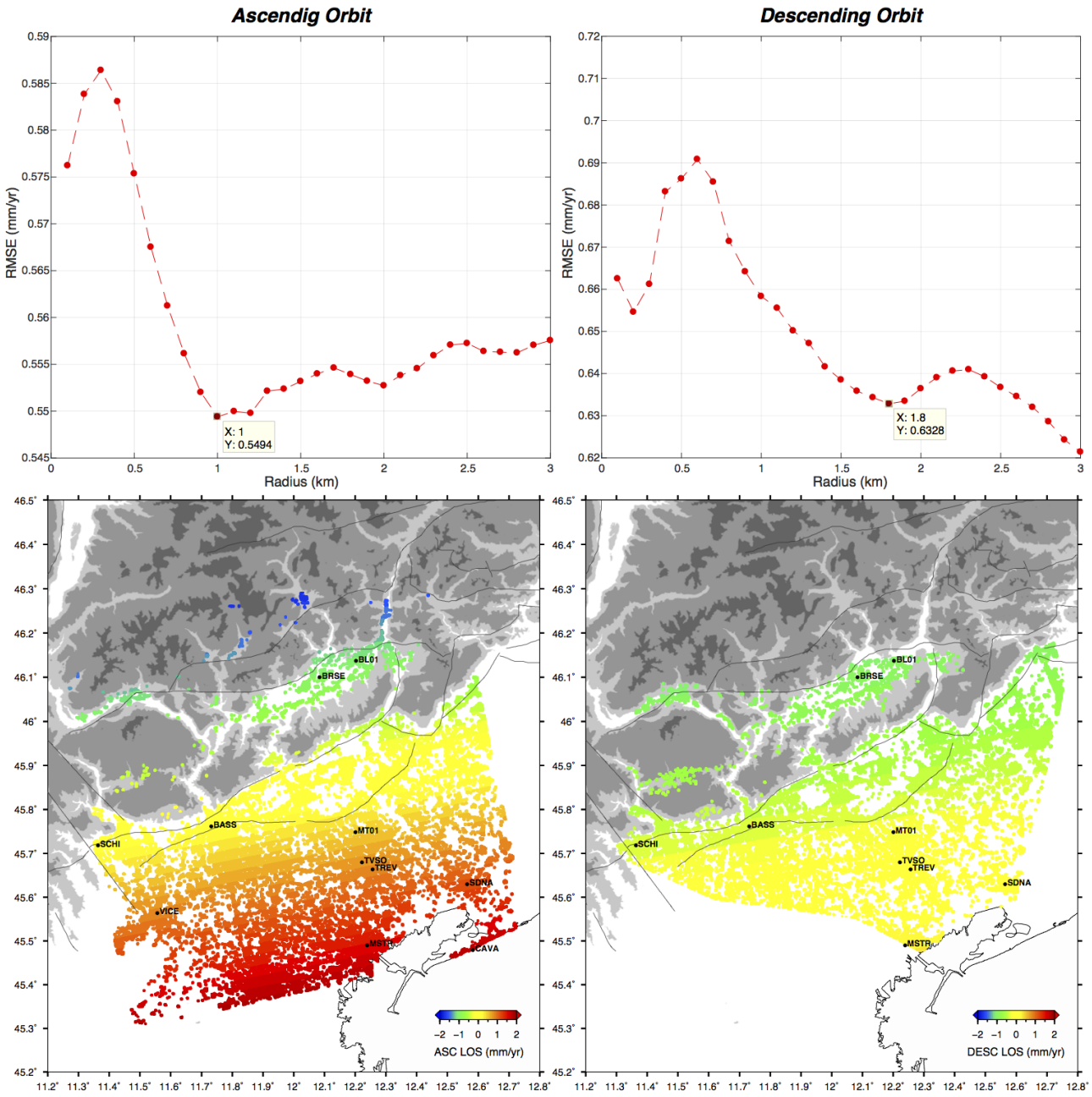

Figure S5 Planar ramp correction for InSAR datasets - Top: RMSE estimate after the planar signal removal for the considered GPS stations (named sites in the bottom panels) varying the neighbouring radius and considering the mean value of InSAR velocities as representative of each point. We choose the radius for which we obtain the minimum of the RMSE, i.e. 1 km for the ascending dataset and 1.8 km for the descending one - Bottom: final planar ramp correction applied to the ascending (left) and descending (right) datasets.

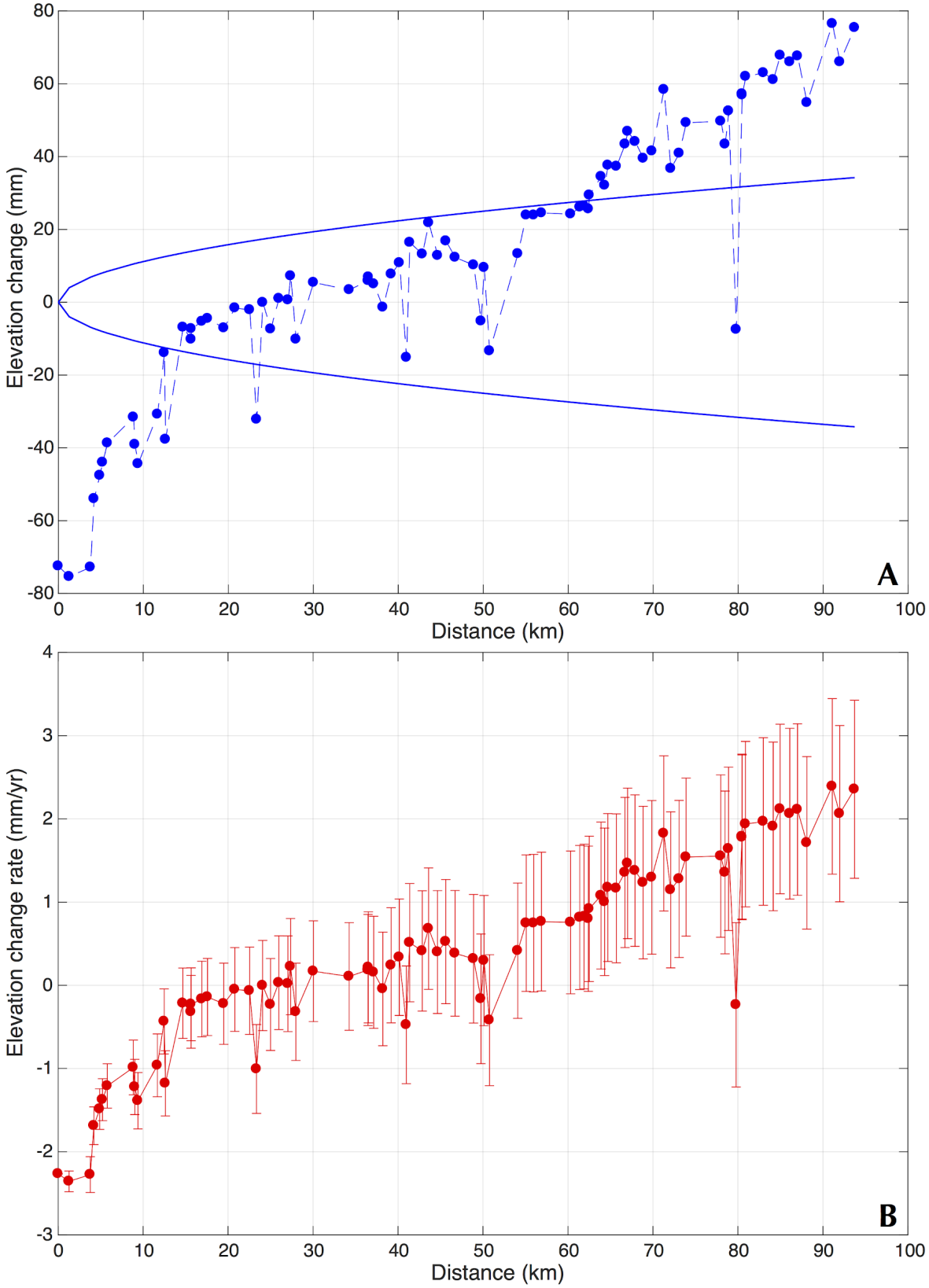

Figure S6 A. Elevation change estimates along the leveling line measured in the time interval 1952-1984 (EC values in Table S2), continuous lines indicate the maximum propagation error allowed following the calculation indicated in Text S3 - B. Elevation change rates from leveling data with associated errors (see Table S2).

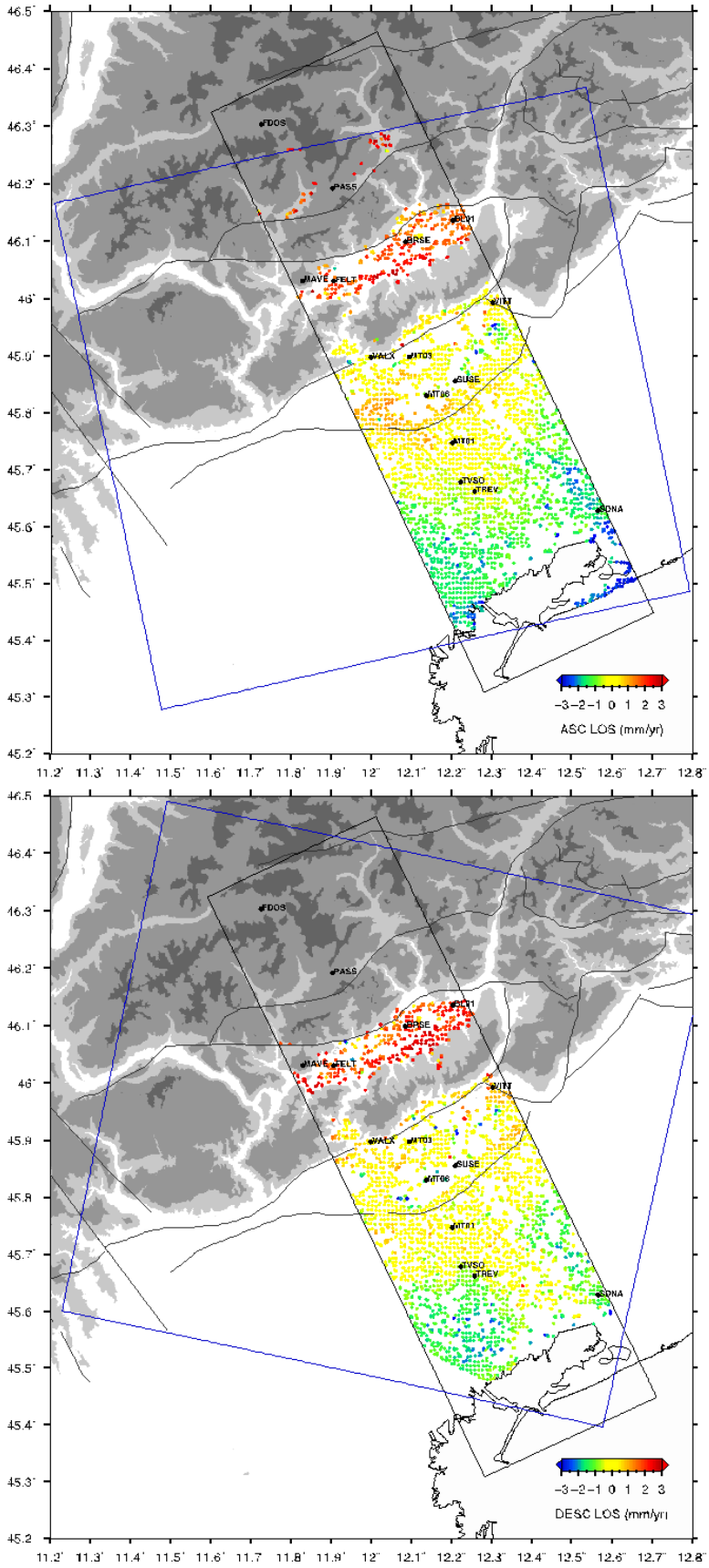

Figure S7 Subsampled DInSAR velocities for both the ascending (top) and descending (bottom) datasets along a 35 km wide transect oriented towards NNW. The reported GPS sites are those used for the dislocation modeling.

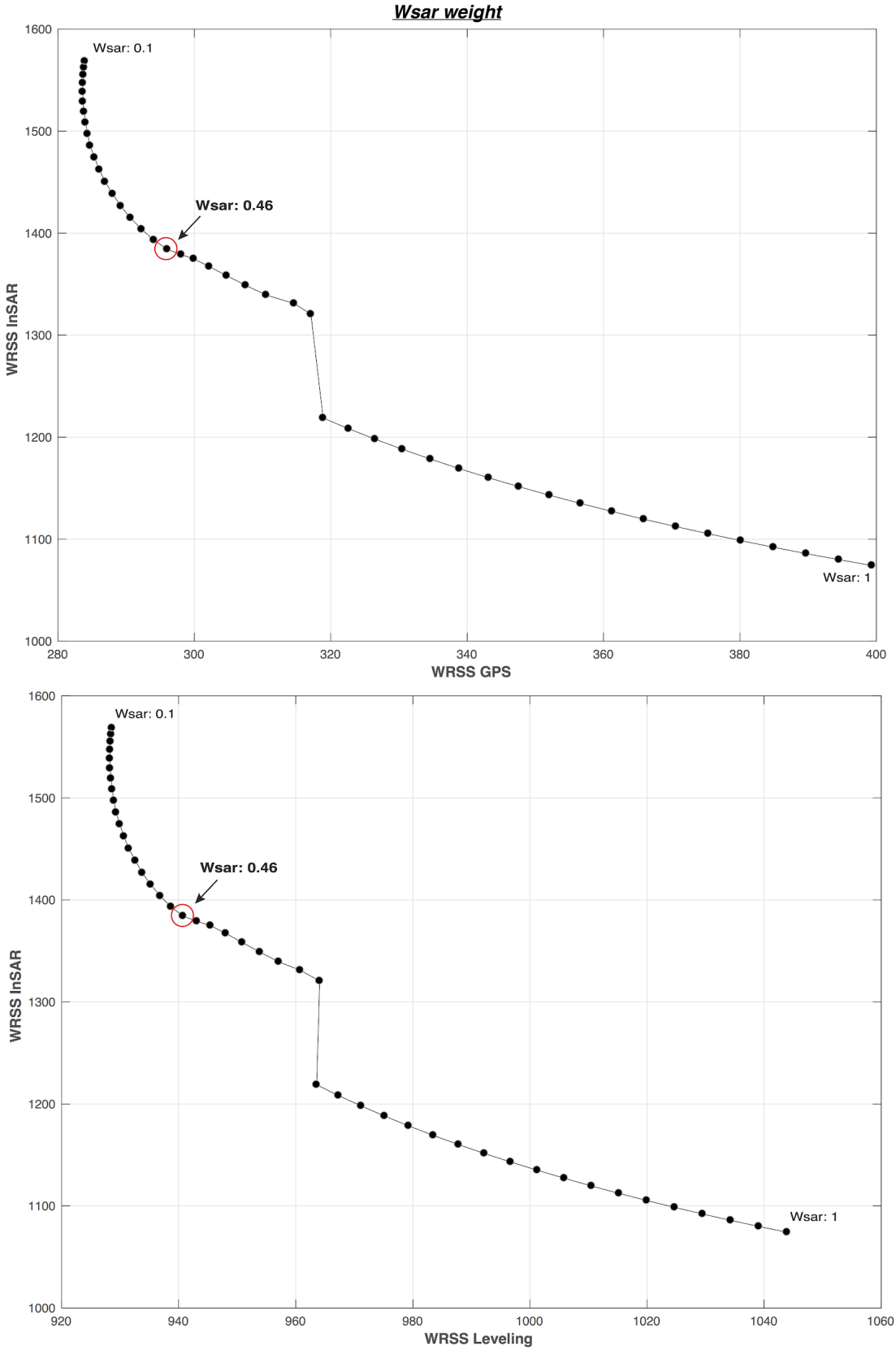

Figure S8 Trade-off curves between Weighted Residuals Sum of Squares (WRSS) of GPS and InSAR data (top) and Leveling and InSAR data (bottom) varying the weighting factor *Wsar* in the interval [0.1-1] with steps of 0.02. The optimal value of *Wsar* 0.46 has been chosen as the "knee point" of the curves.

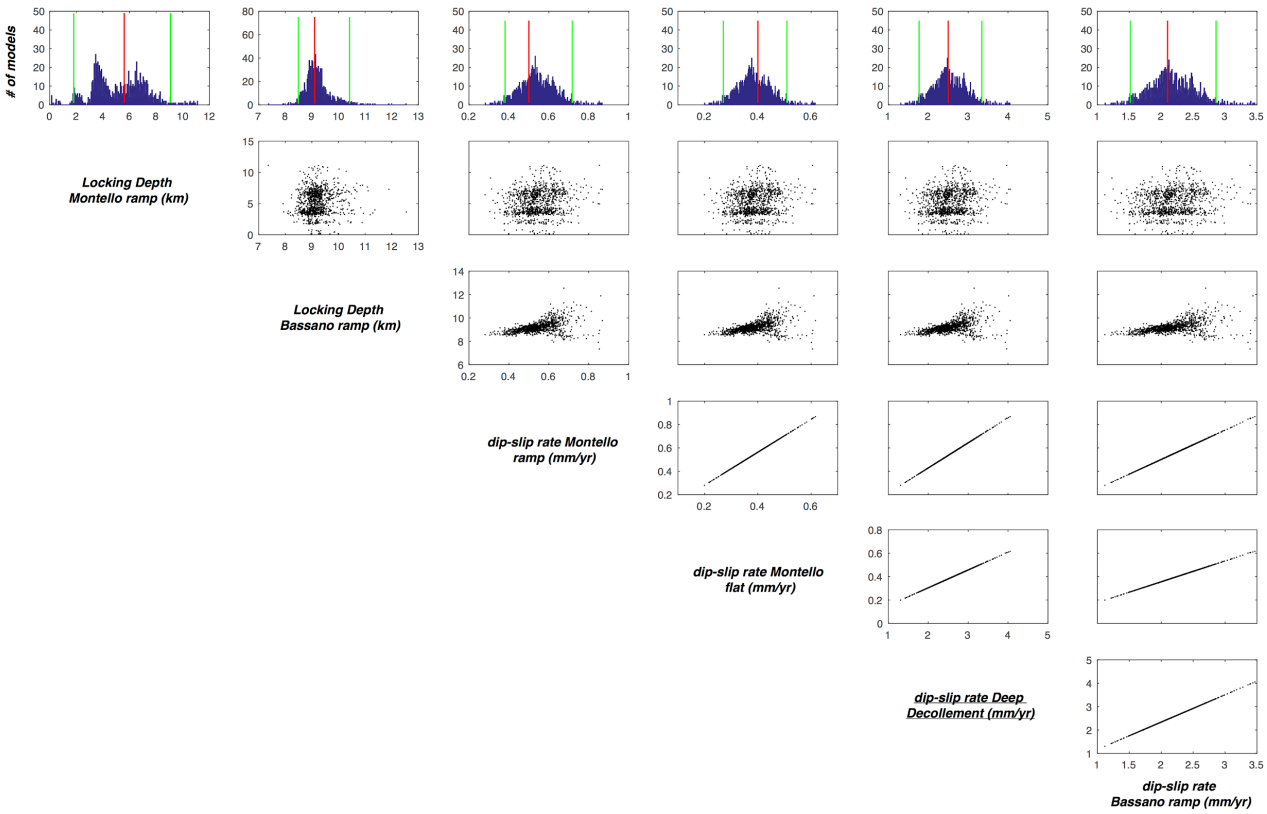

Figure S9 Model parameters distribution, obtained from the inversion of 1000 bootstrap re-samples (e.g. Árnadóttir and Segall, 1994) of the original data (see Section 5). Top row: frequency histograms of the optimal fault parameters with the best optimal model (red line) and bounds values at 95 percentile confidence interval (green lines); see Table 2 for specific values. Other rows: scatter plots showing trade-off between parameter pairs.

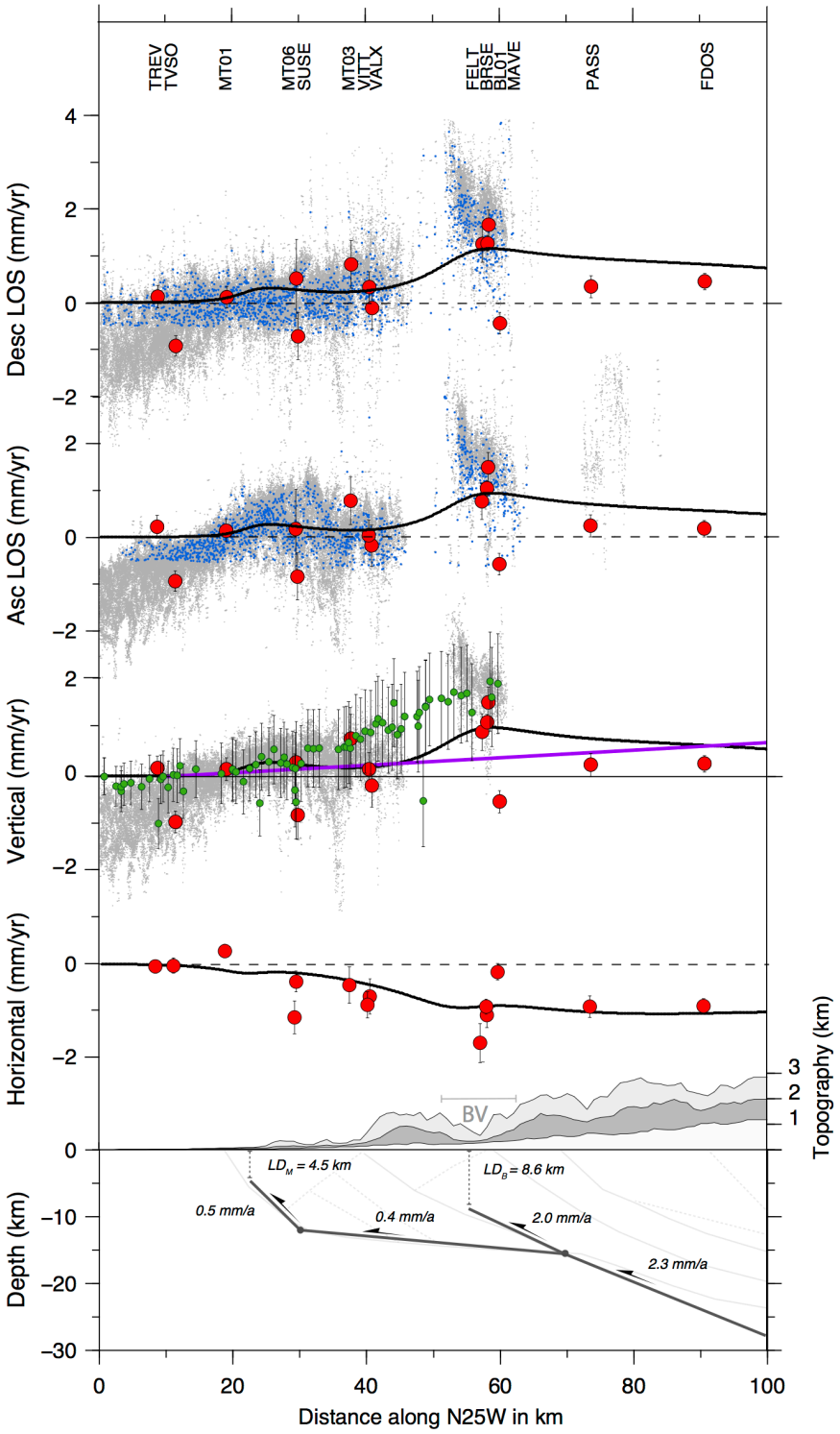

Figure S10 Cross sections, across the A-B profile of Fig. 2 of the manuscript, showing the modeled (black lines) horizontal and vertical velocities, as well as the SAR ascending and descending LoS rates, along with the measured ones corrected for the vertical linear gradient (purple line). Green points indicate leveling data, while red and small blue dots represent GPS and the subsampled InSAR LOS rates, respectively, used during the inversion, displayed along with the un-subsampled InSAR dataset (light gray points). The bottom panel reports the optimal fault geometry with dip-slip rates and locking depths estimates. BV: Belluno valley

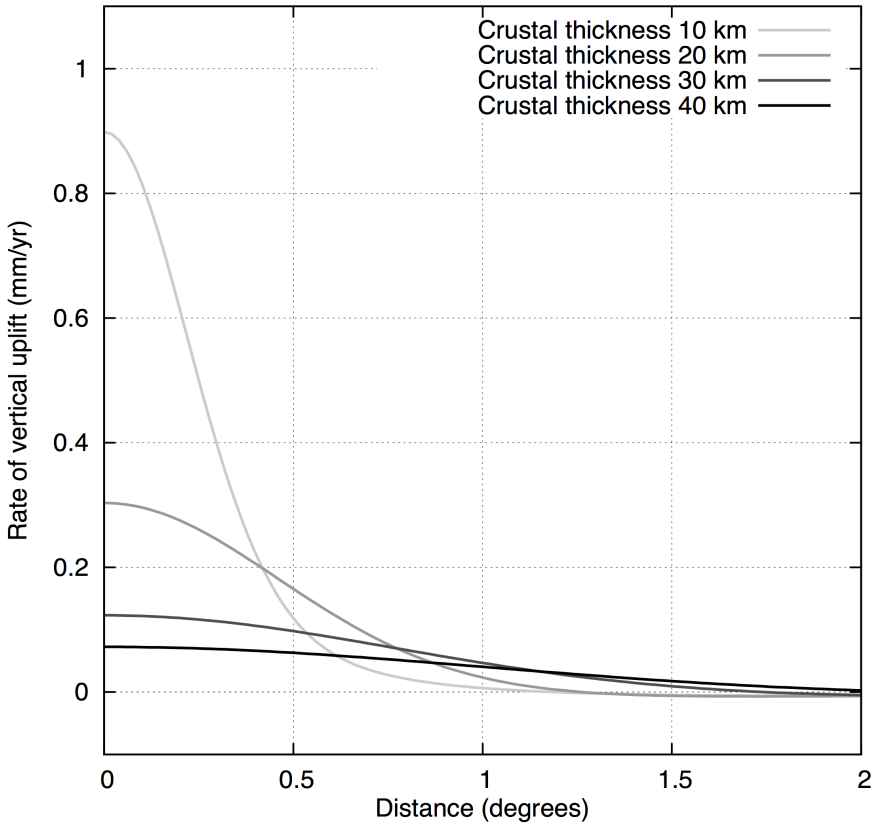

Figure S11 Vertical velocities due to the Piave ice pond melting instantly 10 Kyr ago, modeled as a disk, with a cap profile, of an equivalent area of ~45x15 km^2, 800 m thick. We used an Earth model composed by a crustal layer, a viscosity profile consistent with the ICE5G model (VM2 of Peltier, 2004), with viscosity values of 2.7, 0.5 and 0.5 10^{21} Pa.s in the lower mantle, transition zone and upper mantle, respectively. The model is run at harmonic degrees up to 6000.

Table S1: Horizontal and vertical GPS velocities in a Adria-fixed reference frame.

lon	lat	Ve	Vn	Se	Sn	Ren	Vu	Su	Reu	Run	site	t1	t2
12.7990	46.4147	0.574	-1.243	0.032	0.051	-0.0063	0.820	0.176	0.0717	-0.1707	AMPE_GPS	1999.4013	2017.3821
11.5254	45.8663	0.077	-0.547	0.053	0.053	0.0353	-0.107	0.243	-0.0303	-0.1583	ASIA_GPS	2003.6013	2017.3821
12.5636	46.1931	-0.026	-0.636	0.096	0.093	-0.0570	-0.086	0.389	0.0739	-0.1616	BARC_GPS	2007.8369	2017.3821
11.7314	45.7618	0.520	-0.679	0.084	0.083	0.0011	0.182	0.197	0.0203	-0.1656	BASS_GPS	2007.7712	2014.7219
13.0694	45.6719	0.055	0.258	0.063	0.063	0.0077	-2.177	0.282	0.0005	-0.1178	BEVA_GPS	2008.0368	2017.3821
12.2025	46.1370	0.368	-0.822	0.070	0.082	-0.0109	1.520	0.176	0.0340	-0.1193	BL01_GPS	2008.1816	2017.3821
11.3652	46.4970	0.928	-0.546	0.138	0.121	0.0437	0.056	0.460	-0.0479	-0.0718	BOLZ_GPS	2012.0532	2017.3821
11.2842	45.4007	0.091	-0.422	0.113	0.169	0.0132	-0.753	0.406	0.0391	-0.1352	BONI_GPS	2012.0915	2016.9275
11.9694	45.5329	0.073	-0.213	0.103	0.092	0.0016	0.427	0.730	0.0178	-0.1010	BOR2_GPS	2008.4713	2014.9191
12.2181	46.4372	0.578	-0.924	0.115	0.102	0.1121	0.933	0.312	-0.1024	-0.2098	BORC_GPS	2009.2260	2017.3821
11.0343	45.5998	0.110	-0.154	0.071	0.071	-0.0009	-0.080	0.220	0.0468	-0.1263	BOSC_GPS	2006.1739	2016.9467
12.0841	46.1000	0.286	-1.058	0.115	0.135	-0.0295	1.943	0.328	0.0634	-0.1434	BRSE_GPS	2008.7855	2017.3821
11.2783	45.2578	-0.169	-0.616	0.070	0.083	-0.0050	-1.811	0.334	0.0207	-0.1014	BTAC_GPS	2008.6243	2017.3821
11.3368	46.4990	0.574	-0.804	0.043	0.048	-0.0544	0.987	0.132	0.0283	-0.0740	BZRG_GPS	1998.0013	2017.3821
11.9392	45.6703	0.140	-0.190	0.131	0.089	0.0092	-0.771	0.280	0.0255	-0.1286	CAFV_GPS	2011.1657	2017.3821
12.4350	46.0083	0.363	-0.793	0.115	0.125	-0.0716	-0.051	0.161	0.1306	-0.1663	CANV_GPS	2004.3838	2017.3821
12.5827	45.4794	-0.061	0.498	0.049	0.059	-0.0351	-2.805	0.208	0.0413	-0.1173	CAVA_GPS	2001.5438	2011.1657
12.2655	45.2065	-0.200	-0.262	0.202	0.093	0.0136	-3.373	0.399	0.0212	-0.1334	CGIA_GPS	2010.9630	2017.3821

11.2814	45.5427	0.219	0.029	0.140	0.190	0.0608	0.028	0.409	0.0481	-0.1118	CHI9_GPS	2012.0833	2017.3767
11.7946	45.6395	0.199	0.090	0.091	0.073	-0.0042	-2.571	0.358	0.0301	-0.1289	CITD_GPS	2009.1520	2017.3821
12.9791	45.9585	0.026	0.061	0.054	0.064	-0.0146	-0.624	0.188	0.0301	-0.1330	CODR_GPS	2007.3767	2017.3821
11.7238	46.3039	0.430	-0.779	0.049	0.085	-0.0243	0.893	0.179	0.0217	-0.0821	FDOS_GPS	2006.1657	2017.3821
11.9055	46.0318	0.832	-1.460	0.207	0.206	-0.0032	1.307	0.393	0.0322	-0.1125	FELT_GPS	2012.0751	2017.3821
13.0011	46.4142	0.557	-1.109	0.058	0.083	-0.0579	0.576	0.230	0.1522	-0.1776	FUSE_GPS	2007.6917	2017.3821
12.3850	45.9284	0.152	-0.041	0.097	0.208	0.0116	-1.213	0.417	0.0206	-0.1366	GOD9_GPS	2012.0860	2017.3821
13.4161	46.1840	0.168	-0.549	0.057	0.053	-0.0157	-0.079	0.168	0.0207	-0.1297	JOAN_GPS	2007.4890	2017.3821
11.2685	45.1841	0.162	0.208	0.078	0.084	-0.0282	-1.705	0.201	0.0258	-0.1286	LEGN_GPS	2008.6516	2016.1898
11.6691	45.7483	0.314	-0.377	0.123	0.101	0.0135	-0.749	0.353	0.0115	-0.1527	MARO_GPS	2012.0833	2017.3821
11.8271	46.0321	0.236	-0.065	0.097	0.086	-0.0116	-0.161	0.236	0.0371	-0.1188	MAVE_GPS	2006.3794	2016.9986
13.4356	45.9245	-0.043	0.199	0.035	0.028	-0.0705	-0.283	0.138	0.1068	-0.1859	MDEA_GPS	2003.0643	2017.3821
12.0151	45.9753	0.303	-0.332	0.110	0.165	-0.0273	-0.259	0.337	0.0157	-0.1182	MGRD_GPS	2009.6917	2017.3821
12.0954	45.4976	0.078	0.169	0.133	0.119	0.0117	-0.444	0.352	0.0217	-0.1284	MIRA_GPS	2012.4658	2017.3821
11.1434	46.0981	0.618	-0.371	0.050	0.051	-0.0195	0.949	0.174	0.0391	-0.1246	MOCA_GPS	2006.6972	2017.3821
13.1983	46.4067	0.340	-1.018	0.035	0.070	0.0343	0.783	0.148	-0.0603	-0.1809	MOGG_GPS	1999.4013	2017.3767
12.9877	46.2408	0.054	-0.679	0.061	0.089	-0.0438	-0.038	0.134	0.0967	-0.2029	MPRA_GPS	2003.0205	2017.3821
12.2386	45.4904	-0.244	0.165	0.064	0.107	0.0063	-2.493	0.338	0.0617	-0.1274	MSTR_GPS	2007.8890	2014.6342
12.2006	45.7487	-0.033	0.300	0.056	0.077	-0.0138	0.205	0.242	0.0175	-0.1300	MT01_GPS	2009.2178	2017.3821
12.1699	45.8403	0.071	-0.989	0.149	0.202	0.0878	-1.694	0.822	-0.2207	-0.2608	MT02_GPS	2009.2150	2014.5657
12.0934	45.8988	0.055	-0.458	0.156	0.200	-0.0038	1.004	0.529	0.0431	-0.1781	MT03_GPS	2009.4260	2015.4972
12.1364	45.8313	0.587	-0.974	0.121	0.186	0.0262	0.433	0.877	0.0069	-0.1539	MT06_GPS	2012.0532	2017.3821
12.5884	45.6684	0.968	-0.432	0.120	0.140	-0.0043	-3.217	0.287	0.0253	-0.1335	NOVE_GPS	2009.4013	2017.3821
12.4891	45.7878	0.020	0.169	0.072	0.124	0.0112	-1.259	0.298	0.0203	-0.1362	ODEZ_GPS	2011.1712	2017.3821
11.8961	45.4112	0.128	-0.391	0.042	0.064	-0.0258	-0.319	0.103	0.0259	-0.0949	PADO_GPS	2001.9054	2017.3821
11.1230	45.7769	0.409	-0.277	0.102	0.095	0.1243	0.061	0.270	-0.0415	-0.1671	PARR_GPS	2006.7794	2017.3821
11.9020	46.1930	0.133	-0.931	0.110	0.112	-0.1025	0.735	0.247	0.0529	-0.0553	PASS_GPS	2006.9767	2017.3821
13.0526	45.8057	-0.031	-0.276	0.043	0.045	-0.0227	0.169	0.181	0.0281	-0.0951	PAZO_GPS	2007.9301	2017.3821
11.8793	45.4222	-0.173	-0.198	0.235	0.198	-0.0141	-0.165	0.904	0.0519	-0.1150	PD01_GPS	2007.8506	2010.4890
13.3076	45.9046	-0.285	-0.200	0.043	0.044	-0.0039	0.096	0.120	0.0070	-0.1044	PLMN_GPS	1999.4972	2012.8811
12.6612	45.9568	-0.023	0.041	0.042	0.053	-0.0120	-0.021	0.140	0.0230	-0.0829	PORD_GPS	2002.0013	2017.3821
12.8331	45.7674	0.531	0.284	0.057	0.063	-0.0191	-2.726	0.245	0.0316	-0.1250	PORT_GPS	2007.5273	2017.3821
11.6817	46.4226	0.648	-0.891	0.086	0.082	-0.1284	0.862	0.231	0.0795	-0.1791	POZZ_GPS	2006.7794	2017.3821
12.0299	45.1959	0.255	-0.123	0.079	0.082	0.0213	-0.902	0.232	0.0007	-0.1540	REBO_GPS	2010.3794	2017.2917
11.0421	45.8935	0.164	-0.357	0.055	0.054	-0.0421	0.262	0.229	0.0640	-0.1741	ROVE_GPS	2004.1898	2017.3821
11.0721	45.6469	0.226	-0.350	0.101	0.079	-0.0393	0.107	0.251	0.0039	-0.1220	ROVR_GPS	2008.7718	2017.3821
12.3365	45.4307	0.418	0.069	0.195	0.149	0.0065	-0.950	0.516	0.0202	-0.1396	SAL__GPS	2014.3931	2017.3821
11.1416	46.4187	0.811	-0.501	0.055	0.051	-0.0184	1.306	0.192	0.0310	-0.1229	SARN_GPS	2006.8287	2017.3821
11.3630	45.7181	0.089	0.049	0.070	0.088	-0.0239	0.126	0.284	0.0382	-0.1394	SCHI_GPS	2008.3920	2017.3821
12.5642	45.6298	0.127	-0.189	0.061	0.101	-0.0138	-0.247	0.285	0.0257	-0.0855	SDNA_GPS	2007.4863	2017.3794
11.8020	45.6006	0.253	0.063	0.106	0.145	0.0100	-1.177	0.396	0.0240	-0.1371	SGIO_GPS	2012.0833	2017.3821
11.5094	46.0694	0.177	-0.750	0.060	0.088	-0.0195	0.863	0.203	0.0213	-0.1687	SPER_GPS	2006.7794	2017.3821
12.2085	45.8570	0.216	-0.299	0.122	0.108	0.0333	-0.686	0.520	0.0686	-0.1755	SUSE_GPS	2011.1383	2017.3821
12.3961	46.0605	0.458	-0.216	0.165	0.218	0.0099	-0.161	0.707	0.0459	-0.1486	TAMB_GPS	2011.6808	2017.3821
11.6773	45.3428	-0.240	0.056	0.045	0.044	-0.0412	-0.250	0.208	0.0409	-0.1112	TEOL_GPS	2004.2472	2017.3821
11.1102	46.1023	0.287	0.290	0.128	0.113	0.0324	0.729	0.418	0.0426	-0.1754	TRE8_GPS	2012.0532	2017.3821
12.2217	45.6798	0.111	0.070	0.121	0.120	0.0129	-1.254	0.372	0.0150	-0.1398	TRE9_GPS	2012.0833	2017.3821
11.1183	46.0909	0.761	-0.619	0.082	0.079	0.0387	-0.187	0.215	-0.0518	-0.2216	TREN_GPS	2006.7794	2017.3821
12.2565	45.6639	-0.182	-0.135	0.075	0.069	-0.0182	0.176	0.251	0.0507	-0.1054	TREV_GPS	2004.3319	2011.1657
12.2432	45.6532	-0.053	0.322	0.100	0.102	0.0176	-0.823	0.367	0.0091	-0.1282	TREX_GPS	2011.1712	2017.3821
12.2217	45.6798	0.020	-0.016	0.072	0.080	-0.0426	-0.968	0.230	0.0512	-0.1344	TVSO_GPS	2008.6489	2017.3821
13.2530	46.0375	-0.064	-0.174	0.047	0.052	-0.0229	-0.161	0.183	0.0369	-0.1337	UDI1_GPS	2006.2561	2017.3821
13.2277	46.0552	0.192	0.027	0.083	0.098	0.0002	-0.201	0.278	0.0293	-0.1220	UDI2_GPS	2008.3265	2017.3821
13.2530	46.0372	-0.135	0.816	0.170	0.280	0.0020	0.211	0.564	0.0292	-0.0677	UDIN_GPS	2003.0205	2006.6780
13.2165	46.0831	-0.129	-0.217	0.073	0.080	0.0259	0.313	0.415	-0.0630	-0.1904	UNUD_GPS	2006.1821	2017.3821
11.8779	45.4067	0.222	0.156	0.151	0.185	-0.0871	0.712	0.419	0.0213	-0.0941	UPAD_GPS	1995.0945	2001.8890
11.9976	45.8982	0.068	-0.720	0.143	0.193	0.0560	0.028	0.456	-0.0232	-0.2067	VALX_GPS	2011.1712	2017.3821
12.5653	46.4571	0.757	-0.922	0.295	0.164	-0.0150	0.144	1.470	0.0210	-0.1326	VARM_GPS	2014.0068	2017.3821
12.3578	45.4379	-0.129	0.244	0.138	0.147	-0.0042	-2.273	0.686	-0.0783	-0.2545	VEAR_GPS	2006.1602	2010.7164
11.3667	45.7887	0.222	-0.549	0.097	0.090	0.0772	0.008	0.356	0.0946	-0.0457	VELO_GPS	2009.3493	2017.3821
12.3541	45.4306	0.110	-0.566	0.067	0.100	-0.0318	-1.550	0.213	0.0170	-0.1255	VEN1_GPS	2009.8068	2017.3821

11.0024	45.4447	0.146	-0.480	0.060	0.088	-0.0156	-0.242	0.190	0.0324	-0.0916	VERO_GPS	2006.8013	2017.3821
11.5563	45.5641	0.116	-0.254	0.047	0.063	-0.0361	-0.620	0.264	0.0472	-0.1291	VICE_GPS	2008.6489	2017.3821
12.3014	45.9933	0.506	-0.721	0.116	0.141	0.0186	0.378	0.347	0.0204	-0.1857	VITT_GPS	2011.1849	2017.3821
11.9109	45.3846	-0.163	0.249	0.051	0.050	-0.0285	0.032	0.394	0.0351	-0.1265	VOLT_GPS	2001.5575	2011.1657

Table S2: Vertical ground motion rates (i.e Elevation Change, EC, rates) estimated from the IGM elevation measurements performed in the 1952-3 and in the 1984-5 leveling campaigns, where *nbcm* is the benchmark number, *dist* indicates the distance from the first benchmark and the errors have been calculated following the formulas presented in Text S2.

nbcm	dist (km)	long	lat	1952-3 (m)	1984-5 (m)	EC (mm)	EC error (mm)	EC_rate (mm/yr)	EC_rate_sig (mm/yr)
0	0	12.2233	45.4764	3.9672	3.8947	-72.50	0.0000	-2.2656	0.0000
1	1.28	12.2222	45.4858	5.0708	4.9954	-75.40	4.0000	-2.3563	0.1250
2	3.78	12.238	45.5006	2.8441	2.7713	-72.80	6.8739	-2.2750	0.2148
3	4.21	12.2386	45.5061	4.2709	4.2169	-54.00	7.2543	-1.6875	0.2267
4	4.89	12.2388	45.5106	5.8518	5.8042	-47.60	7.8182	-1.4875	0.2443
5	5.22	12.2391	45.5139	4.1567	4.1127	-44.00	8.0777	-1.3750	0.2524
6	5.79	12.2386	45.5178	6.9893	6.9506	-38.70	8.5073	-1.2094	0.2659
7	8.85	12.2366	45.5442	6.8699	6.8383	-31.60	10.5178	-0.9875	0.3287
8	9.02	12.2358	45.5494	6.0162	5.9771	-39.10	10.6184	-1.2219	0.3318
9	9.39	12.2352	45.5528	8.4444	8.4	-44.40	10.8340	-1.3875	0.3386
10	11.68	12.2358	45.5692	8.0962	8.0654	-30.80	12.0830	-0.9625	0.3776
11	12.48	12.2341	45.5778	8.4539	8.44	-13.90	12.4900	-0.4344	0.3903
12	12.62	12.2338	45.5778	9.265	9.2273	-37.70	12.5599	-1.1781	0.3925
13	14.68	12.2358	45.5958	13.4197	13.4128	-6.90	13.5462	-0.2156	0.4233
14	15.64	12.2344	45.6028	14.8071	14.7969	-10.20	13.9821	-0.3188	0.4369
15	15.65	12.2344	45.6028	14.9285	14.9212	-7.30	13.9866	-0.2281	0.4371
16	16.91	12.2372	45.6083	10.813	10.8077	-5.30	14.5387	-0.1656	0.4543
17	17.58	12.2391	45.6186	11.2075	11.203	-4.50	14.8240	-0.1406	0.4632
18	19.49	12.2411	45.6358	14.9831	14.976	-7.10	15.6085	-0.2219	0.4878
19	20.79	12.2444	45.6481	14.6418	14.6402	-1.60	16.1206	-0.0500	0.5038
20	22.53	12.2463	45.6656	17.0483	17.0462	-2.10	16.7817	-0.0656	0.5244
21	23.35	12.2561	45.6653	11.0334	11.0012	-32.20	17.0843	-1.0063	0.5339
22	24.07	12.2499	45.6708	16.0511	16.051	-0.10	17.3457	-0.0031	0.5421
23	25	12.2516	45.6789	14.4759	14.4685	-7.40	17.6777	-0.2313	0.5524
24	25.97	12.258	45.6883	18.4302	18.4312	1.00	18.0174	0.0313	0.5630
25	27.04	12.2597	45.695	19.8531	19.8537	0.60	18.3848	0.0188	0.5745
26	27.35	12.2599	45.6992	22.2282	22.2354	7.20	18.4899	0.2250	0.5778

27	27.98	12.2599	45.7036	22.8142	22.804	-10.20	18.7016	-0.3188	0.5844
28	30.04	12.2558	45.7214	28.8918	28.8972	5.40	19.3778	0.1688	0.6056
29	34.25	12.2522	45.7578	48.202	48.2054	3.40	20.6912	0.1063	0.6466
30	36.47	12.2586	45.7767	52.8135	52.8194	5.90	21.3512	0.1844	0.6672
31	36.51	12.2597	45.7769	56.4738	56.4807	6.90	21.3629	0.2156	0.6676
32	37.13	12.2594	45.7822	55.2555	55.2605	5.00	21.5436	0.1563	0.6732
33	38.21	12.2558	45.7914	58.1218	58.1204	-1.40	21.8546	-0.0438	0.6830
34	39.19	12.2536	45.8	64.4865	64.4942	7.70	22.1331	0.2406	0.6917
35	40.15	12.2505	45.8086	67.3459	67.3567	10.80	22.4026	0.3375	0.7001
36	40.98	12.2491	45.8142	72.4976	72.4824	-15.20	22.6329	-0.4750	0.7073
37	41.37	12.253	45.8178	72.9978	73.0142	16.40	22.7404	0.5125	0.7106
38	42.85	12.2572	45.83	67.5596	67.5728	13.20	23.1436	0.4125	0.7232
39	43.6	12.2558	45.8369	70.8439	70.8657	21.80	23.3452	0.6813	0.7295
40	44.65	12.2513	45.8453	74.7978	74.8106	12.80	23.6247	0.4000	0.7383
41	45.62	12.2513	45.8503	77.3346	77.3514	16.80	23.8799	0.5250	0.7462
42	46.71	12.2633	45.8589	64.9263	64.9386	12.30	24.1635	0.3844	0.7551
43	48.89	12.2805	45.8728	60.3113	60.3215	10.20	24.7209	0.3188	0.7725
44	49.76	12.2886	45.8789	58.8121	58.8069	-5.20	24.9399	-0.1625	0.7794
45	50.12	12.2908	45.8803	59.3332	59.3427	9.50	25.0300	0.2969	0.7822
46	50.76	12.2999	45.8839	63.9551	63.9417	-13.40	25.1893	-0.4188	0.7872
47	54.09	12.3302	45.9019	66.447	66.4603	13.30	26.0024	0.4156	0.8126
48	55.08	12.3255	45.9103	70.0553	70.0792	23.90	26.2393	0.7469	0.8200
49	55.96	12.3216	45.9175	75.2025	75.2264	23.90	26.4481	0.7469	0.8265
50	56.88	12.3224	45.9256	80.4213	80.4458	24.50	26.6646	0.7656	0.8333
51	60.31	12.3249	45.9553	103.1457	103.1699	24.20	27.4568	0.7563	0.8580
52	61.39	12.3249	45.9633	107.0572	107.0833	26.10	27.7015	0.8156	0.8657
53	61.9	12.3202	45.9653	107.4331	107.4595	26.40	27.8164	0.8250	0.8693
54	62.4	12.3147	45.9697	114.1532	114.1788	25.60	27.9285	0.8000	0.8728
55	62.5	12.3169	45.9675	112.8119	112.8413	29.40	27.9508	0.9188	0.8735
56	63.89	12.3083	45.9758	123.8826	123.9171	34.50	28.2600	1.0781	0.8831
57	64.31	12.3047	45.9814	127.7338	127.7659	32.10	28.3527	1.0031	0.8860
58	64.69	12.2961	45.9856	138.3567	138.3943	37.60	28.4363	1.1750	0.8886
59	65.69	12.2936	45.9931	143.6824	143.7197	37.30	28.6553	1.1656	0.8955
60	66.71	12.2919	46.0003	141.5122	141.5556	43.40	28.8769	1.3563	0.9024
61	67.02	12.2913	46.0031	141.5246	141.5715	46.90	28.9439	1.4656	0.9045
62	67.89	12.2888	46.0094	157.0616	157.1057	44.10	29.1312	1.3781	0.9103
63	68.85	12.2905	46.0181	164.6513	164.6908	39.50	29.3364	1.2344	0.9168
64	69.87	12.2955	46.0256	168.5418	168.5833	41.50	29.5529	1.2969	0.9235
65	71.28	12.3033	46.0306	186.9851	187.0435	58.40	29.8496	1.8250	0.9328

66	72.09	12.3111	46.0383	230.2242	230.2609	36.70	30.0187	1.1469	0.9381
67	73.08	12.3099	46.0433	286.2116	286.2525	40.90	30.2242	1.2781	0.9445
68	73.9	12.3149	46.05	285.9962	286.0455	49.30	30.3933	1.5406	0.9498
69	77.97	12.3349	46.0756	444.0567	444.1064	49.70	31.2190	1.5531	0.9756
70	78.48	12.3361	46.0775	427.211	427.2544	43.40	31.3209	1.3563	0.9788
71	78.9	12.3374	46.0792	489.1689	489.2214	52.50	31.4046	1.6406	0.9814
72	79.79	12.3358	46.0847	454.0982	454.0907	-7.50	31.5812	-0.2344	0.9869
73	80.48	12.333	46.0875	433.4771	433.5343	57.20	31.7175	1.7875	0.9912
74	80.49	12.333	46.0875	431.0088	431.0657	56.90	31.7195	1.7781	0.9912
75	80.9	12.3299	46.0919	407.2951	407.3571	62.00	31.8002	1.9375	0.9938
76	82.99	12.3274	46.1092	390.602	390.665	63.00	32.2083	1.9688	1.0065
77	84.15	12.3241	46.1178	395.9218	395.9829	61.10	32.4326	1.9094	1.0135
78	84.97	12.3197	46.1253	386.2923	386.3601	67.80	32.5903	2.1188	1.0184
79	86.1	12.318	46.135	385.2408	385.3068	66.00	32.8062	2.0625	1.0252
80	87.01	12.3199	46.1447	385.5099	385.5775	67.60	32.9792	2.1125	1.0306
81	88.11	12.3202	46.1522	387.5125	387.5673	54.80	33.1870	1.7125	1.0371
82	91.1	12.303	46.1733	391.7877	391.8642	76.50	33.7454	2.3906	1.0545
83	91.98	12.2938	46.1728	398.1984	398.2644	66.00	33.9080	2.0625	1.0596
84	93.72	12.2833	46.1789	402.5926	402.668	75.40	34.2272	2.3563	1.0696

Table S3: Parameters used for the subsampling of the ascending and descending InSAR datasets, whose definition is reported in Text S3

Orbit	***Tp***	***Np***	***R***	div_{lon}	div_{lat}	n_{crit}	***final pixel***
Asc	101273	2500	25%	10	10	1000	2679
Desc	85474	2500	38%	9	9	1050	2343

References

Altamimi, Z., Collilieux, X., Métivier, L., 2011. ITRF2008: an improved solution of the international terrestrial reference frame. J Geodesy 85, 457–473. doi:10.1007/s00190-011-0444-4.

Árnadóttir, T., Segall, P., 1994. The 1989 Loma Prieta earthquake imaged from inversion of geodetic data. Journal of Geophysical Research: Solid Earth 99, 21835–21855. doi:10.1029/94JB01256.

Blewitt, G., Lavallée, D., 2002. Effect of annual signals on geodetic velocity. J Geophys Res 107, 2145. doi:10.1029/2001JB000570.

Boehm, J., Werl, B., Schuh, H., 2006. Troposphere mapping functions for GPS and very long baseline interferometry from European Centre for Medium-Range Weather Forecasts operational analysis data. J Geophys Res 111. doi:10.1029/2005JB003629.

Costantini, M. 1998. A novel phase unwrapping method based on network programming. IEEE Trans. Geosci. Remote Sens., 36, 3, 813-821, DOI: 10.1109/36.673674

D'Anastasio, E., De Martini, P.M., Selvaggi, G., Pantosti, D., Marchioni, A., Maseroli, R., 2006. Short-term vertical velocity field in the Apennines (Italy) revealed by geodetic levelling data. Tectonophysics 418, 219–234, doi:10.1016/j.tecto.2006.02.008

Dong, D., Herring, T., King, R., 1998. Estimating regional deformation from a combination of space and terrestrial geodetic data. J Geodesy 72, 200–214.

Dong, D., Fang, P., Bock, Y., Cheng, M., Miyazaki, S., 2002. Anatomy of apparent seasonal variations from GPS-derived site position time series. J Geophys Res-Sol Ea 107, –. doi:10.1029/2001JB000573.

Dong, D., Fang, P., Bock, Y., Webb, F., Prawirodirdjo, L., Kedar, S., Jamason, P., 2006. Spatiotemporal filtering using principal component analysis and Karhunen-Loeve expansion approaches for regional GPS network analysis. Journal of Geophysical Research: Solid Earth 111, doi:10.1029/2005JB003806

Goldstein, R., Werner, C., 1998. Radar interferogram filtering for geophysical applications. Geophysical Research Letter, 25, 21, 4035-4038, DOI: 10.1029/1998GL900033.

Herring, T. A., King, R. W., Floyd, M. A., McClusky, S. C., 2015. Introduction to GAMIT/GLOBK, Release 10.6. Retrieved from http://www-gpsg.mit.edu/~simon/gtgk/Intro_GG.pdf.

Lagler, K., Schindelegger, M., Böhm, J., Krásná, H., & Nilsson, T., 2013. GPT2: Empirical slant delay model for radio space geodetic techniques. Geophysical Research Letters, 40, 1069–1073. https://doi.org/10.1002/grl.50288.

Lyard, F., Lefevre, F., Letellier, T., & Francis, O., 2006. Modelling the global ocean tides: Modern insights from FES2004. Ocean Dynamics, 56(5-6), 394–415. https://doi.org/10.1007/s10236-006-0086-x .

Pasquali, P., Cantone, A., Riccardi, P., Defilippi, M., Ogushi, F., Gagliano, S., Tamura, M., 2014. Mapping of ground deformations with interferometric stacking techniques, Land Application of Radar Remote Sensing, Holecz, F., Pasquali, P., Milisavljevic, N., Closson, D., IntechOpen, DOI: 10.5772/58225. Available online

Peltier, W.R. 2004. Global glacial isostasy and the surface of the ice-age Earth: the ICE-5G (VM2) model and GRACE. Annual Review of Earth and Planetary Sciences 2004 32:1, 111-149, doi:10.1146/annurev.earth.32.082503.144359.

Schmid, R., Rothacher, M., Thaller, D., Steigenberger, P., 2005. Absolute phase center corrections of satellite and receiver antennas. GPS Solut 9, 283–293. doi:10.1007/s10291-005-0134-x.

Schmid, R., Steigenberger, P., Gendt, G., Ge, M., Rothacher, M., 2007. Generation of a consistent absolute phase-center correction model for GPS receiver and satellite antennas. J Geodesy 81, 781–798. doi:10.1007/s00190-007-0148-y.

Serpelloni, E., Casula, G., Galvani, A., Anzidei, M., Baldi, P., 2006. Data analysis of permanent GPS networks in Italy and surrounding regions: application of a distributed processing approach. Ann Geophys-Italy 49, 897–928.

Serpelloni, E., Faccenna, C., Spada, G., Dong, D., Williams, S.D.P., 2013. Vertical GPS ground motion rates in the Euro-Mediterranean region: New evidence of velocity gradients at different spatial scales along the Nubia-Eurasia plate boundary. J Geophys Res-Sol Ea 118, 6003–6024. doi:10.1002/2013JB010102.

Sternai P., Sue, C., Husson, L., Serpelloni, E., Becker, T.W., Willett, S.D., Faccenna, C., Di Giulio, A., Spada, G., Jolivet, L., Valla, P., Petit, C., Nocquet, J.-M., Walpersdorf, A., and Castelltort, S., 2019. Present-day uplift of the European Alps: Evaluating mechanisms and models of their relative contributions, Earth-Science Reviews, 190, 589–604, doi:10.1016/j.earscirev.2019.01.005.

Vignal, J., 1936. Evaluation de la precision d'une methode de nivellement. Bull. Geod., 49, 1–159. Vignal, J., 1950. Comptes rendus des séances de travail de la Secion II. Nivellments, de l'Assocation Internationale de Géodésie à l'Assemblée Générale d'Oslo (Aout 1948). Bull. Géod. 18, 401–565.